

Efficient Generation of Multimodal Fluid Simulation Data

Daniele Baieri¹ Donato Crisostomi¹ Stefano Esposito² Filippo Maggioli³ Emanuele Rodolà¹

Abstract

In this work, we introduce an efficient generation procedure to produce synthetic multi-modal datasets of fluid simulations. The procedure can reproduce the dynamics of fluid flows and allows for exploring and learning various properties of their complex behavior, from distinct perspectives and modalities. We employ our framework to generate a set of thoughtfully designed training datasets, which attempt to span specific fluid simulation scenarios in a meaningful way. The properties of our contributions are demonstrated by evaluating recently published algorithms for the neural fluid simulation and fluid inverse rendering tasks using our benchmark datasets. Our contribution aims to fulfill the community’s need for standardized training data, fostering more reproducible and robust research.

1. Introduction

Applying the representational power of machine learning to the prediction of complex fluid dynamics has been a relevant subject of study for years and is regarded today as an established research field (Lino et al., 2023). However, the amount of available fluid simulation data does not match the notoriously high requirements of machine learning methods. Researchers have typically addressed this issue by generating their own datasets, as in the case of Pfaff et al. (2021) and Ummenhofer et al. (2020), only to cite a few. Such an heterogeneous distribution of training data across different methods prevents a consistent comparison of the proposed approaches.

This work introduces a generation procedure for synthetic multi-modal fluid simulations datasets. By leveraging a GPU implementation, our procedure is efficient enough that no data needs to be exchanged between users, except for

¹Department of Computer Science, Sapienza University of Rome, Italy ²Autonomous Vision Group, University of Tuebingen, Germany ³Department of Computer Science, University of Milano-Bicocca, Italy. Correspondence to: Daniele Baieri <baieri@di.uniroma1.it>.

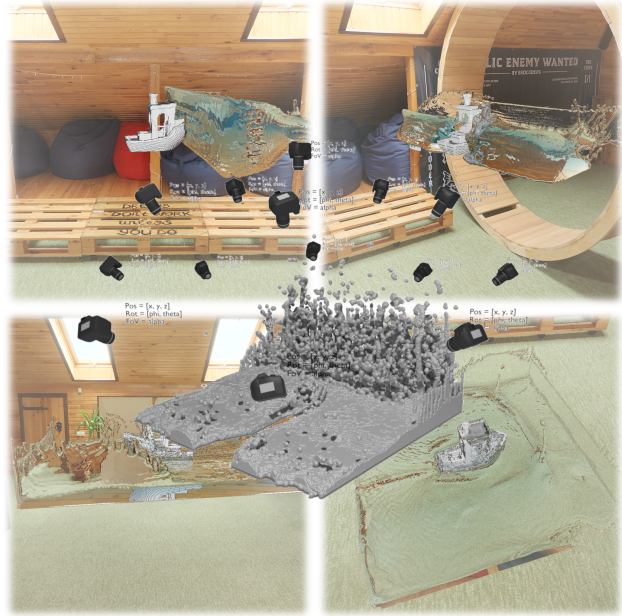


Figure 1: Our generation tool performs Lattice Boltzmann simulation steps, exporting the fluid geometry and rendering output frames from multiple viewpoints. Camera positions are sampled with Fibonacci sphere sampling (Keinert et al., 2015), and exported as metadata.

configuration files required to reproduce the dataset. Furthermore, our procedure allows multiple modalities (generating both geometries and photorealistic renderings) and is general enough for it to be applied to various tasks in data-driven fluid simulation.

Recent advancements in animation datasets have significantly enhanced data-driven models, streamlining traditional computer graphics challenges and expanding digital artists’ creative possibilities. Notably, skeleton-based animation datasets, supported by specialized data capture technology, have become prevalent due to their diverse applications. Prominent examples include DFAUST (Bogo et al., 2017) for human body animations and DeformingThings4D (Li et al., 2021) for various subjects. One really successful application of human motion datasets was the creation of SMPL (Loper et al., 2015), a skinned multi-person linear model, which may be used for traditional skinning as well

as in a generative fashion, to sample novel human poses and styles. However, capturing intricate fluid deformations contrasts sharply, necessitating specialized, expensive, and labor-intensive tools (Hoyer et al., 2005; Eckert et al., 2019). This complexity restricts the diversity of fluid motion data, prompting the creation of synthetic datasets to encompass a broader spectrum of fluid behaviors.

Our dataset is constructed using a flexible template that is customizable through a configuration file, defining variables and constants such as initial fluid states, boundary conditions, and simulation parameters. The template is expandable to incorporate extra features like initial velocities or dynamic force fields. Scenes are generated by varying these parameters and simulated using a highly efficient GPU-based Lattice Boltzmann method (Lehmann), enabling rapid large-scale dataset creation. Additionally, users can select multiple viewpoints for photorealistic renders and choose the fluid geometry’s export format, accommodating both Eulerian and Lagrangian simulation data.

Our dataset holds potential for various research areas. We demonstrate its utility in two key domains that have garnered considerable attention: advancing data-driven fluid simulation models (Ummenhofer et al., 2020; Werhahn et al., 2019) and tackling inverse rendering/surface recovery (Li et al., 2023; Chu et al., 2022).

Overall, our work aims to bridge a long-standing gap in data-driven fluid simulation research, enhancing community contributions, reproducibility, and systematic evaluation. Our key contributions are:

- introducing an efficient GPU-based framework for generating synthetic, multi-modal fluid simulation data, capturing diverse fluid dynamics representations (see Figure 1);
- using this framework, we provide three training datasets for distinct fluid simulation scenarios, setting a benchmark for consistent research assessments;
- demonstrating the effectiveness of our datasets by successfully training state-of-the-art models for fluid simulation and inverse rendering tasks.

2. Motivation and applications

Our dataset could substantially aid efforts integrating neural networks with fluid dynamics simulation, offering new research avenues. Notably, it supports fluid super-resolution, where models learn to enhance low-resolution simulations into detailed, high-resolution outputs. GAN models have been notably effective in this area (Werhahn et al., 2019; Xie et al., 2018), improving super-resolution in scenarios like smoke flow upsampling and turbulence prediction (Bai

et al., 2020; 2021). Further research extends this approach to complex scenarios like multi-phase flows (Li & McComb, 2022) and label-free super-resolution (Gao et al., 2021). This methodology also shows promise in simulating biological systems, indicating its broad applicability (Ferdian et al., 2020).

More in general, one could exploit neural networks to learn the entire simulation model using the current fluid state as input, adopting either Lagrangian or Eulerian perspectives. The Lagrangian approach focuses on particle-based fluid dynamics. Continuous convolution on point sets has been shown to yield efficient and robust models (Ummenhofer et al., 2020). Enhancements include momentum conservation (Prantl et al., 2022) and applying graph neural networks to particle-based models (Li & Farimani, 2022), improving performance without sacrificing quality. Conversely, the Eulerian viewpoint treats fluids and properties (like velocity) as functions over space. Innovations here include generative models for velocity fields (Kim et al., 2019) and using latent spaces in generative models to produce stable and controllable simulations (Wiewel et al. (2019; 2020)). We refer to Vinuesa & Brunton (2022) for a comprehensive review of learning paradigms in fluid simulation.

More recent research explores NeRF’s inverse rendering technique (Mildenhall et al., 2020) in fluid dynamics. Chu et al. (2022) first integrated Navier-Stokes principles into 4D NeRF training, developing a dual-network model enforcing physical constraints to accurately reconstruct smoke density with limited camera views. NeuroFluid (Guan et al., 2022) built on this, adopting a Lagrangian approach and incorporating physics constraints into volume rendering for model optimization. Li et al. (2023) combined Eulerian and Lagrangian methods, achieving remarkable versatility across diverse materials. However, these approaches overlook real-world fluid material properties, treating color as a mere surface texture. NeReF (Wang et al., 2022) addressed this by formulating a NeRF that considers reflective and transmissive materials, enabling realistic light-fluid interactions, notably in transparent fluids like water.

A prevalent problem in the cited research is the absence of a standardized benchmark dataset, leading researchers to create new simulation datasets for method evaluation. Our generation tool addresses this by enabling: a) export of fluids as both particles and density fields, b) multi-view renderings of simulations, and c) efficient dataset regeneration using a configuration file, eliminating the need to distribute massive data volumes.

3. Related work

Our dataset, while not the first in fluid simulation data, differs significantly from prior works like the Johns Hopkins

Turbulence Databases (JHTD) (Perlman et al., 2007; Li et al., 2008; Graham et al., 2016). JHTD offers extensive, high-resolution data on turbulent flows, targeting geophysical and engineering applications like meteorology and aerodynamics. However, its massive scale and detail, with thousands of frames and billions of voxels per frame, render it less suitable for computer graphics and vision applications. In contrast, our contribution is designed with practicality and adaptability for CG/CV purposes.

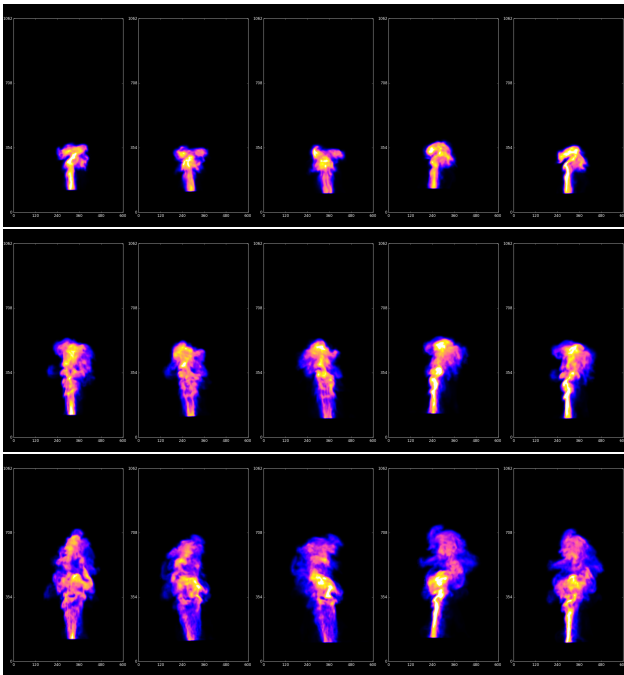


Figure 2: Multiple rendered views for three timesteps of a smoke plume simulation from the ScalarFlow (Eckert et al., 2019) dataset. The rendered density field is reconstructed from real smoke captures.

Many datasets accompanying data-driven simulation studies have limitations. Pfaff et al. (2021)’s work, using graph neural networks (Scarselli et al., 2008) on triangle meshes, was confined to 2D due to planar mesh limitations in representing 3D volumes. EAGLE dataset (Janny et al., 2023), also mesh-based, focused on turbulent wind dynamics influenced by boundary shapes. Stachenfeld et al. (2022) introduced volumetric datasets across different dimensions, modeling real-world chaotic systems. However, our dataset is specifically tailored for fluid dynamics in computer graphics, offering additional visual data. Notably, datasets from Ummenhofer et al. (2020), initially minor contributions, later became foundational for training methods like those in Prantl et al. (2022).

The work most similar in spirit to ours is ScalarFlow (Eckert et al., 2019). This is a collection of video captures of real-world smoke plumes dynamics (see Figure 2), coupled with

density field reconstructions of the corresponding volumetric data computed by an algorithm proposed by the authors. Despite ScalarFlow being a large scale dataset (ca. 26 billion voxels of data), its scope is limited to the real-world capture setting set up by the authors; when using real data over synthetic would provide no significant advantage, our generation framework could provide similar data in arbitrary quantities, without the additional cost of capture.

Recent proposals by Toshev et al. (2023); Toshev & Adams (2023) provided contributions in similar, albeit complementary, directions to our own: their LagrangeBench tool and data allow to systematically and reproducibly test pre-trained neural Lagrangian simulation models on small synthetic benchmark datasets consisting of well-known simulation settings. Such efforts further highlight the demand for such resources in the field. Combining these efforts could create a comprehensive pipeline for training and evaluating neural Lagrangian simulation models. Lastly, we mention that large-scale simulation data is widely used beyond fluid dynamics, notably in garment animation. Two notable examples from this field are the datasets presented in CLOTH3D (Bertiche et al., 2020) and TailorNet (Patel et al., 2020).

4. Dataset

In this section, we outline our data generation process, providing high-level implementation details. For comprehensive documentation, please refer to our code release at [see-anonymized-supplementary-material](#). We use this procedure to create two mid-scale training datasets for data-driven fluid simulation and a set of scenes for fluid inverse rendering algorithms.

4.1. Data generation

Our C++ code library refactors the FluidX3D Lattice-Boltzmann GPU simulator (Lehmann). This was chosen considering its a) impressive efficiency on mid-range hardware, b) built-in ray-traced rendering capabilities, and c) wide compatibility with several operating systems and GPU architectures due to its OpenCL kernel implementation. We retained the core implementation and improved the API to expose most functionalities via a generic `Scene` class. These objects represent the simulation’s initial state and parameters, facilitating fine-grained configuration and inheritance for extending base behavior. For instance, initial fluid shapes and boundary conditions can be provided through input mesh files, which are adjustable in translation, rotation, and scaling. Enabling specialized features like point-wise external force fields or inflows/outflows requires overriding basic `Scene` functionalities.

The refactored implementation serves as a library for defining dataset-specific `Scene` subclasses, which can be ac-

Listing 1: JSON configuration file for our generation procedure. Variables are sampled and aggregated in order to generate configuration files for individual instances in the dataset. Fluid bodies and solid obstacles can be specified both as constants and variables, and sampled according to specific properties of geometric primitives or meshes (*e.g.*, center, scale, rotation).

```

"export_root": "path/to/out/dir",
"seed": 123456,
"constants": {
  "sim_params": {
    "Nx": 256, "Ny": 256, "Nz": 256,
    ...
  },
  "obstacles": {
    ...
  },
  ...
},
"variables": {
  "sim_params": {
    "nu": {
      "type": "linscale",
      "vmin": 0.0005, "vmax": 0.005, "steps": 20
    },
    "sigma": {
      "type": "normal",
      "mean": 0.001, "std": 0.0005, "nsamples": 20
    }
  },
  "fluids": [
    ...
  ]
}
    
```

cessed through an executable file. These subclasses are entirely configurable using a simple JSON file (see Listing 1). Using this framework, we implemented the generation procedure as a Python script that creates configuration files and feeds them to the simulation tool. The script takes various input parameters, including global generation parameters like the seed for reproducibility. It also requires a set of constants and variables. Constants are preserved in generated instances, while the variables are sampled based on their selected type, which includes linear intervals, uniform distributions, normal distributions, collections, and more complex structures. Users can also set a maximum scene count, in which case scene instances are uniformly sampled from all possible combinations of variables. This configuration is easily supplied via a separate JSON file.

During simulation, specific frames can be extracted both as multi-view renderings and geometric information. For rendering efficiency, we employ a specialized FluidX3D algorithm that balances speed over photorealism. It limits camera ray bounces to two and uses the mean of material BSDF, rather than sampling them; this way, the light interactions of the water material we use for fluids can still be displayed, while the rendering procedure remains really fast, being executed on the GPU (see Section 5.2). For geometric data extraction, we offer two options. The first exports fluid as a binary particle array, with the number of particles determined by the configuration file input. The second exports

the fluid’s density field as a memory-efficient 3D matrix in sparse coordinate format (COO), stored as a 1D binary array. Despite the latter method being very memory-efficient (see Section 5.2), selecting a specific number of particles may be more convenient at high resolutions. We provide a Python loader to Numpy arrays for both file formats.

4.2. Datasets

4.2.1. COHERENT SUBSETS OF SIMULATION SPACE

The first application we present for the procedure we described in Section 4.1 is devoted to the generation of collections of “similar” (in a fluid dynamics sense) simulations, regardless of the scale of such collections. To this end, we introduce two medium scale benchmark datasets based on well-known fluid dynamics settings. Throughout this section, we will refer to 3D coordinate systems assuming that the up-axis is the z direction.

Our first training dataset (`obstacles`) consists of simulations displaying a sphere of fluid colliding with varying boundary geometries under the effect of gravity. We define a cubic boundary $B = (\mathbf{p}, \mathbf{q})$ enveloping the entire scene, where $\mathbf{p}_{\{x,y,z\}}$ and $\mathbf{q}_{\{x,y,z\}}$ are the min/max coordinate values for the vertices of B , respectively. We represent the initial fluid state by a sphere $S = (\mathbf{c}, r)$ and the solid obstacle as a triangle mesh $M = (V, F)$, which we can instantiate by sampling its center, rotation and size (\mathbf{o}, θ, s) . In order to ensure interaction between the two, we set $\mathbf{c}_x = \mathbf{o}_x = (\mathbf{q}_x - \mathbf{p}_x)/2$ and $\mathbf{c}_y = \mathbf{o}_y = (\mathbf{q}_y - \mathbf{p}_y)/2$. We sample the radius $r \sim \mathcal{U}(r_{\min}, r_{\max})$ and mesh size $s \sim \mathcal{U}(s_{\min}, s_{\max})$ as the maximum dimension of its bounding box. Since we want the fluid above the obstacle to ensure interaction, we sample the two in the top/bottom halves of the simulation domain, respectively. Thus, we sample:

$$\mathbf{c}_z \sim \mathcal{U}\left(\frac{\mathbf{q}_z - \mathbf{p}_z}{2} + r_{\max}, \mathbf{q}_z - r_{\max}\right) \quad (1)$$

$$\mathbf{o}_z \sim \mathcal{U}\left(\mathbf{p}_z + \frac{s_{\max}}{2}, \frac{\mathbf{q}_z - \mathbf{p}_z}{2} - \frac{s_{\max}}{2}\right), \quad (2)$$

where we choose $r_{\min}, r_{\max}, s_{\min}$, and s_{\max} to be, respectively, the 10%, 20%, 25% and 45% of $\mathbf{q}_z - \mathbf{p}_z$. Lastly, we randomly rotate M along x to augment the dataset with additional unique boundary interactions, *i.e.*, $\theta_x \sim \mathcal{U}(0, \frac{\pi}{2})$. The geometry of the mesh (V, F) is chosen randomly from a small collection of 5 shapes with varying complexity.

The second dataset, which we refer to as `dam-break`, is a collection of instances of this well-known fluid dynamics scenario. In this setting, a cuboid of fluid is placed in contact with the lower face of a cubic boundary $B = (\mathbf{p}, \mathbf{q})$, and simulated under the effect of gravity. The only variable for our scene generation procedure is the initial placement of the dam inside the scene: if we represent the cuboid by its

Table 1: Real-world scale of the `obstacles` and `dam-break` datasets. Legend: $\delta x, \delta m, \delta t \rightarrow$ space, mass and time units (respectively). $\nu \rightarrow$ kinematic shear viscosity. $\sigma \rightarrow$ surface tension. $\rho \rightarrow$ density. $g \rightarrow$ gravitational acceleration. $Re_{\max} \rightarrow$ upper bound for the Reynolds number of the simulations.

	Real	LBM
δx	$7.81 \cdot 10^{-3} [m]$	1
δm	$4.76 \cdot 10^{-4} [kg]$	1
δt	$4.45 \cdot 10^{-4} [s]$	1
ν	$2.00 \cdot 10^{-3} [m^2/s]$	$1.46 \cdot 10^{-2}$
σ	$7.20 \cdot 10^{-2} [kg/s^2]$	$3.00 \cdot 10^{-4}$
ρ	$1.00 \cdot 10^3 [kg/m^3]$	1
g	$9.81 [m/s^2]$	$2.49 \cdot 10^{-4}$
Re_{\max}	10119	10119

center and sides, *i.e.*, $D = (\mathbf{c}, \mathbf{s})$, we set the y coordinates to span the entire y -axis ($\mathbf{s}_y = \mathbf{q}_y - \mathbf{p}_y, \mathbf{c}_y = \mathbf{s}_y/2$) and sample the x coordinates as

$$\mathbf{c}_x \sim \mathcal{U}(\mathbf{p}_x + \delta_x, \mathbf{q}_x - \delta_x) \quad (3)$$

$$\mathbf{s}_x \sim \mathcal{U}(s_x^{\min}, \min\{\mathbf{c}_x, \mathbf{N}_x - \mathbf{c}_x\}), \quad (4)$$

where we set s_x^{\min} and δ_x to the 10% and the 25% of $\mathbf{q}_x - \mathbf{p}_x$, respectively. For the z coordinates, since we require the dam to touch the ground, we only sample the center

$$\mathbf{c}_z \sim \mathcal{U}\left(\mathbf{p}_z + \delta_z, \frac{\mathbf{q}_z - \mathbf{p}_z}{2}\right) \quad (5)$$

and set $\mathbf{s}_z = 2(\mathbf{c}_z - \mathbf{p}_z)$, where δ_z is set to the 25% of $\mathbf{q}_z - \mathbf{p}_z$.

We choose physical properties of the fluid to achieve: a) reasonable space/time scale, b) water-like behavior, c) stability of the simulation. The resulting real world scale, coupled with the corresponding LBM units, is detailed in Table 1. We fix the simulation domain to have characteristic length $L = 2[m]$ in all dimensions, and select density and surface tension values to be identical to those of water. To obtain the remaining quantities, we need to fix the simulation resolution; we choose $\mathbf{N} = (256, 256, 256)$, which we observed to yield a reasonable tradeoff between quality and efficiency. From the fixed data, we obtain $\delta x = L/\max\{\mathbf{N}\}$, and $\delta m = \rho \cdot \delta x^3$. To determine the timestep, we fix the surface tension in LBM units and obtain $\delta t = \sqrt{\sigma_{\text{real}}/\sigma_{\text{LBM}}} \cdot \delta m$. The value is empirically chosen to obtain a reasonable time scale. In this setting, using the real kinematic shear viscosity of water (10^{-6}) would dramatically increase the Reynolds number $Re_{\max} = (\min\{\mathbf{N}\} \cdot \mathbf{u}_{\max})/\nu_{\text{LBM}}$ (where $\mathbf{u}_{\max} = 1/\sqrt{3}$ in LBM) of our simulations, yielding turbulent flows which can make the simulation unstable. Therefore, we reduce the viscosity to keep the maximum Reynolds

Table 2: Generation data for our neural fluid simulation datasets. We aim for an output resolution of 50FPS, therefore we export one frame every 0.02s of simulation (equivalently, 42 LBM steps with the δt in Table 1). The resulting throughput proves the efficiency of our procedure: allowing for a 10% decay in performance, we could be able to generate a massive 1mln frames dataset (ca. $16 \cdot 10^{12}$ voxels of data with the same settings) in ~ 45 hours.

Dataset	dam-break	obstacles
Generation time (s)	15253	14654
Throughput (FPS)	6.55	6.82
Sampled scenes	200	400
t_{\max} (s)	10.0	5.0
Frame count	100.000	100.000
Frame time (s)	0.02	0.02
Size (GB)	23.2	17.5
Particles	5000	3000

number around 10^4 , which we verified ex-post to yield stable simulations.

We give complete details on the generation of the two datasets in Table 2.

4.2.2. HAND-CRAFTED MULTI-VIEW SCENES

Additionally, we used our generation procedure to simulate a limited set of hand-crafted scenes, primarily intended for training inverse rendering and surface recovery algorithms. These scenes are not designed to cover a wide spectrum of fluid behaviors but rather serve as challenging test cases to assess the generalizability and accuracy of novel methods. Details about the `ship` scene’s data are summarized in Figure 1, and comprehensive information on real-world scale and simulation for each scene is provided in Table 3.

We simulate all scenes with resolution $\mathbf{N} = (256, 256, 256)$ and export at 60FPS. 10 viewpoints are sampled in the upper hemisphere via Fibonacci sphere sampling (Keinert et al., 2015), and each output frame is rendered with resolution 1080×1080 twice, once with a water-like material and once with a Lambertian material. For each camera, a background-only render is also produced, and the camera parameters for the viewpoints are exported as JSON. The data totals 20.32GB.

4.2.3. COPYRIGHT INFORMATION

Along with our dataset, we redistribute a small set of meshes and HDRI environment textures which we used to make our datasets more interesting. All such content was obtained from polyhaven.com under CC-0 copyright license (no rights reserved).

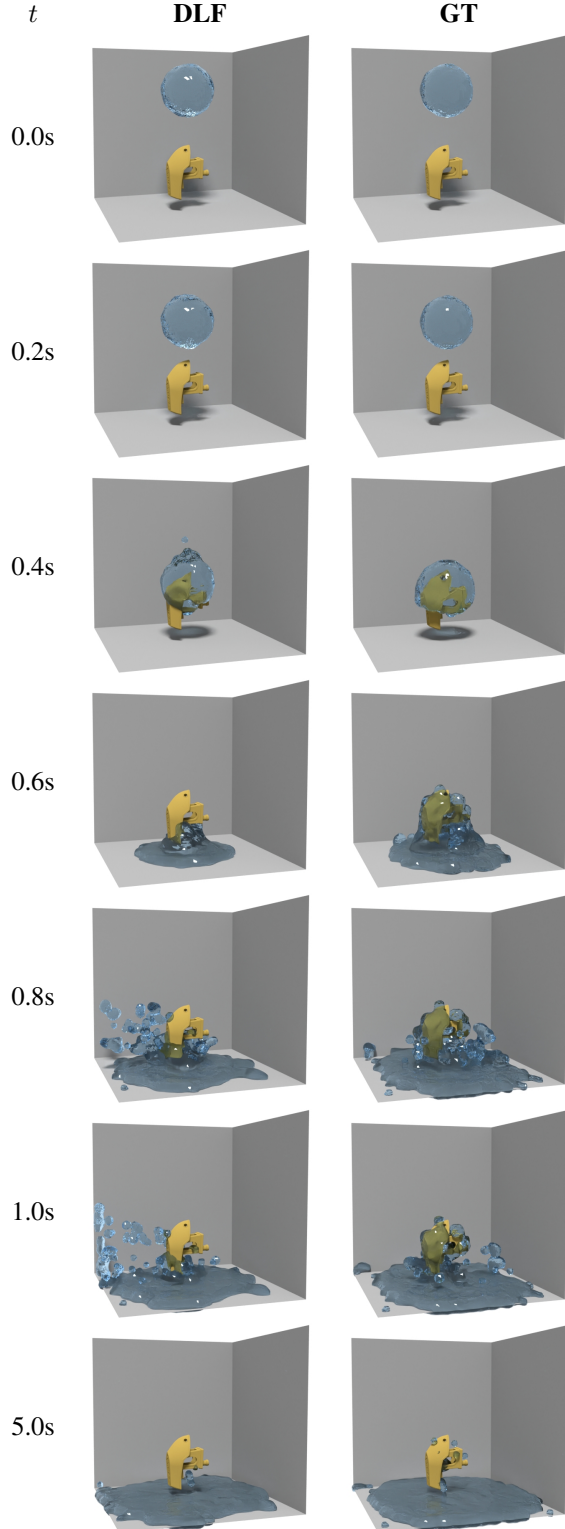


Figure 3: Samples extracted from a 50 frames rollout of a DLF (Ummenhofer et al., 2020) model trained on our obstacles dataset, with unseen initial conditions, compared to the ground truth LBM simulation.

Table 3: Generation time and real-world scale for the scenes in our inverse rendering dataset. ρ and g are as in Table 1 for all scenes. We fix the reference real world $\sigma = 0.072 [kg/s^2]$ and vary the LBM coefficient for surface tension.

Scene	ball	dam	duck	ship
t_{\max} (s)	1.5	2.5	1.5	2.5
Frame count	90	150	90	150
L [m]	2.0	2.0	2.0	2.0
δx [m]	$7.81 \cdot 10^{-3}$	$7.81 \cdot 10^{-3}$	$7.81 \cdot 10^{-3}$	$7.81 \cdot 10^{-3}$
δm [kg]	$4.76 \cdot 10^{-4}$	$4.76 \cdot 10^{-4}$	$4.76 \cdot 10^{-4}$	$4.76 \cdot 10^{-4}$
δt [s]	$8.13 \cdot 10^{-4}$	$2.57 \cdot 10^{-4}$	$8.13 \cdot 10^{-4}$	$8.13 \cdot 10^{-4}$
ν [m^2/s]	$5 \cdot 10^{-4}$	$2 \cdot 10^{-3}$	$5 \cdot 10^{-2}$	$5 \cdot 10^{-3}$
σ [LBM]	$1 \cdot 10^{-4}$	$1 \cdot 10^{-5}$	$1 \cdot 10^{-4}$	$1 \cdot 10^{-4}$
Re_{\max}	22170	17527	222	2217

5. Evaluation

5.1. Examples of applications

5.1.1. DATA-DRIVEN FLUID SIMULATION

In this section, we test the suitability of the datasets described in Section 4.2.1 to train a data-driven model.

Model Ummenhofer et al. (2020) aims to understand fluid mechanics by studying particle motion. In particular, a continuous convolutional network is fed with a collection of particles, each paired with its features. Each particle is associated with a feature vector that is a constant scalar of 1, paired with the particle’s velocity, denoted by \mathbf{v} , and its viscosity, ν . Therefore, at any timestep n , a particle p_i^n is represented by the tuple $(\mathbf{x}_i^n, [1, \mathbf{v}_i^n, \nu_i])$. To compute the intermediate velocities and positions and integrate external force information for the network, the velocity is listed as an input feature. Using Heun’s method, the intermediate velocities \mathbf{v}_i^{n*} and positions \mathbf{x}_i^{n*} commencing from timestep n are then computed as:

$$\mathbf{v}_i^{n*} = \mathbf{v}_i^n + \Delta t \mathbf{a}_{\text{ext}} \quad (6)$$

$$\mathbf{x}_i^{n*} = \mathbf{x}_i^n + \Delta t \frac{\mathbf{v}_i^n + \mathbf{v}_i^{n*}}{2} \quad (7)$$

where \mathbf{a}_{ext} represents an acceleration vector, enabling the application of external forces like fluid control or gravity. These intermediate values are devoid of any particle or scene interactions; such interactions are incorporated using the ConvNet. For the network to manage collisions, another group of static particles s_j are introduced. These are sampled along scene boundaries and paired with normals \mathbf{n}_j as their feature vectors, expressed as $s_j = (\mathbf{x}_j, [\mathbf{n}_j])$. The network performs the function:

$$[\Delta \mathbf{x}_1, \dots, \Delta \mathbf{x}_N] = \text{ConvNet} \left(\{p_i^{n*}\}_{i=1}^N, \{s_i\}_{i=1}^M \right), \quad (8)$$

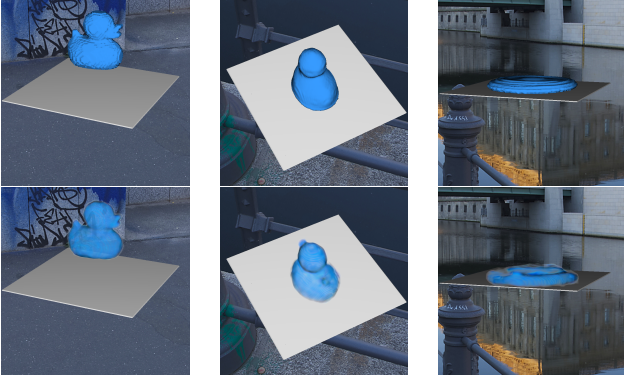


Figure 4: Top: a subset of the views in our duck scene training data. Bottom: PAC-NeRF (Li et al., 2023) reconstruction and rendering for the same (unseen) views (the background is not learned by the model, so it was manually composited for this visualization).

employing convolutions to merge features from both sets of particles. Here, $\Delta \mathbf{x}$ serves as a position correction, factoring in all particle interactions, including collisions with the scene boundary. The correction is finally used to update positions and velocities for timestep $n + 1$ with:

$$\mathbf{x}_i^{n+1} = \mathbf{x}_i^{n*} + \Delta \mathbf{x}_i \quad (9)$$

$$\mathbf{v}_i^{n+1} = \frac{\mathbf{x}_i^{n+1} - \mathbf{x}_i^n}{\Delta t} \quad (10)$$

We refer to this model as *Deep Lagrangian Fluids* (DLF).

Experiment and results We train DLF over obstacles, split as train and validation sets with a 90:10 ratio, which amounts to 360 training simulations (tot. 90k frames) and 40 validation simulations (tot. 10k frames). Figure 3 shows a qualitative comparison of the model prediction vs. the ground truth simulation, after training DLF to convergence (50,000 total iterations), given an initial state from the validation set. The model is able to consistently predict realistic dynamics throughout the simulation, and reach a stable state coherent with the one shown in the data, proving our data to be suitable for this application; the only shortcoming of the learned model is its inability to properly capture viscous behavior, probably due to the viscosity not being explicitly modeled in its formulation (Equations (6) to (10)).

5.1.2. INVERSE RENDERING FLUID SIMULATIONS

Our method allows generating multi-view video data for inverse rendering, consisting of image-pose pairs over time. By defining a Δt and a set of randomly sampled cameras on the upper hemisphere (see Figure 1), we render the scene from these viewpoints during simulation. While our data can be used to train various NeRF-based models, both static

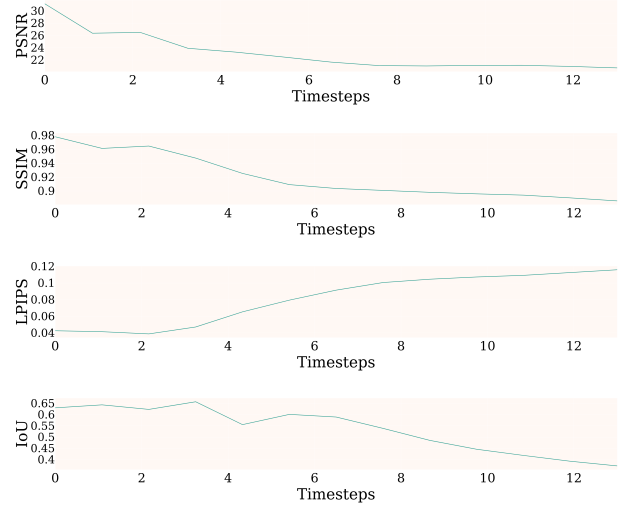


Figure 5: PAC-NeRF evaluation on duck. Both rendering quality and IoU over occupancy grids degrade as the simulation progresses because the neural radiance field reconstruction gets increasingly constrained by the physics-based losses. Note that the image metrics are computed only on the masked foreground object.

and dynamic, we tested them on PAC-NeRF (Li et al., 2023). PAC-NeRF recovers explicit geometric representations and physical properties of dynamic objects in scenes by combining neural scene representations with differentiable physics engines for continuum materials.

A dynamic NeRF comprises time-dependent volume density field $\sigma(\mathbf{x}, t)$ and a time-and-view-dependent appearance (color) field $\mathbf{c}(\mathbf{x}, \omega, t)$ for each point $\mathbf{x} \in \mathbb{R}^3$, and directions $\omega = (\theta, \phi) \in \mathbb{S}^2$ (spherical coordinates). The appearance $\mathbf{C}(\mathbf{r}, t)$ of a pixel specified by ray direction $\mathbf{C}(\mathbf{r}, t)$ ($s \in [s_{\min}, s_{\max}]$) is obtained by differentiable volume rendering (Mildenhall et al., 2020):

$$\mathbf{C}(\mathbf{r}, t) = \mathbf{c}_{bg} T(s_f, t) + \int_{s_n}^{s_f} T(s, t) \sigma(\mathbf{r}(s), t) \mathbf{c}(\mathbf{r}(s), \omega, t) ds \quad (11)$$

$$T(s, t) = \exp\left(-\int_{s_n}^s \sigma(\mathbf{r}(\bar{s}), t) d\bar{s}\right) \quad (12)$$

The dynamic NeRF can therefore be trained to minimize the rendering loss:

$$\mathcal{L}_{\text{render}} = \frac{1}{N} \sum_{i=0}^{N-1} \frac{1}{|\mathcal{R}|} \sum_{\mathbf{r} \in \mathcal{R}} \left\| \mathbf{C}(\mathbf{r}, t_i) - \hat{\mathbf{C}}(\mathbf{r}, t_i) \right\|^2 \quad (13)$$

where N is the number of frames of videos, $\hat{\mathbf{C}}(\mathbf{r}, t_i)$ is the ground truth color observation.

PAC-NeRF first initializes an Eulerian voxel field over the first frame of the sequence. It then uses a grid-to-particle conversion method to obtain a Lagrangian particle field; this is advected, enforcing that the appearance and volume density fields admit conservation laws characterized by the velocity field \mathbf{v} of the underlying physical system:

$$\frac{D\sigma}{Dt} = 0, \quad \frac{Dc}{Dt} = 0 \quad (14)$$

with $\frac{D\phi}{Dt} = \frac{\partial\phi}{\partial t} + \mathbf{v} \cdot \nabla\phi$ being the material derivative of an arbitrary time-dependent field $\phi(\mathbf{x}, t)$. Moreover, the velocity field must obey momentum conservation for continuum materials:

$$\rho \frac{D\mathbf{v}}{Dt} = \nabla \cdot \mathbf{T} + \rho \mathbf{g} \quad (15)$$

where ρ is the physical density field, \mathbf{T} is the internal Cauchy stress tensor, and \mathbf{g} is the acceleration due to gravity and it is evolved using a differentiable Material Point Method (MPM) (Hu et al., 2018). The advected field is then mapped back to the Eulerian domain using the particle-to-grid conversion and is used for collision handling and neural rendering. We refer to the original paper for more technical details.

Experiment and results We trained PAC-NeRF on `duck` by subsampling a 1s simulation of 1800 frames down to 13 frames with a Δt of $\approx 0.077s$. Figure 4 visually confirms that our model generates accurate renders of simulations, validating our multi-view data generation for use in inverse rendering techniques within fluid dynamics. PAC-NeRF applies stricter advection constraints to the NeRF model compared to other 4D NeRF methods. This enhances scene dynamics recognition and yields smoother, more realistic inter-frame reconstructions. However, it may compromise the supervised frame reconstruction quality over time, as depicted in Figure 5, unlike other 4D NeRF methods which maintain stable reconstruction quality but may result in less physically accurate interpolations between simulation steps.

5.2. Generation performance

We assess our generation tool’s efficiency, demonstrating that its GPU implementation allows rapid dataset creation. This speed negates the need to share bulky data, as users can replicate any dataset quickly using just the JSON configuration with our tool.

We provide data about the generation of our `obstacles` and `dam-break` datasets in Table 2. All scenes are rendered from a single viewpoint at low resolution (800×800), to offer a visual support to the generated data. Our procedure reaches a throughput of ~ 6.5 frames per second, allowing to generate 100,000 frames of data in ~ 4 hours. We further analyze our procedure’s runtime and memory occupancy by collecting performance data over multiple runs,

Table 4: Analysis of resource consumption in terms of CPU memory, GPU memory, scene size and time, varying rendering and simulation resolution. Values are averaged over 20 repeated runs over the `dam` scene from the multi-view dataset. Rendering is disabled while gathering the simulation data. Geometry is exported in sparse density format.

Rendering resolutions	800 × 800	FHD	2K	4K
CPU Memory (MB)	374.4	374.4	374.4	374.4
GPU Memory (MB)	1242.4	1244.4	1246.4	1248.4
Scene size (MB)	780.35	861.44	912.94	983.42
Time (s)	16.97	20.46	21.13	22.48
Simulation resolutions	64 ³	128 ³	256 ³	512 ³
CPU Memory (MB)	5.6	46.8	374.4	2995.2
GPU Memory (MB)	148.6	270.8	1242.4	9015.2
Scene size (MB)	11.12	83.12	653.2	4110.02
Time (s)	5.59	7.82	16.05	112.8

changing the simulation resolution and the rendering resolution. The results are reported in Table 4: exploiting GPU programming massively benefits both the simulation and rendering steps, so much so that rendering 150 frames even in 4K only accounts for 28% of the total computation time. Furthermore, this motivates our choice of sparse format for storing density fields: while 4GB per scene may seem a lot at simulation resolution 512, the dense counterpart would require about 80GB per scene ($150 \cdot 512^3$ floats), *i.e.*, we only require 5% of the disk memory.

All generations were run on medium/high-end consumer hardware, to further solidify the claim that our data can be re-generated locally, without the need for sharing entire datasets. Our machine runs Windows 11 over 32GB of DDR4 RAM, an intel core i7 12700K CPU (3.6GHz, 12 physical processors, 20 logical processors), and a NVIDIA RTX4070Ti GPU (7680 CUDA cores). The data was generated on an SSD drive to minimize disk latency.

6. Conclusions

Our work introduces an efficient method for generating multimodal fluid simulation data and three benchmark datasets for research. We detail the generation process and software tool interface, achieving a generation speed of 6.5FPS on consumer-grade hardware, facilitating the creation of large-scale datasets efficiently. We demonstrate the utility of our approach by using our datasets to train neural models for data-driven fluid simulation and fluid inverse rendering, validating its value to the research community.

7. Impact Statement

This paper presents work whose goal is to advance the field of Machine Learning, specifically the application of data-

driven models towards the understanding of complex natural phenomena such as fluid dynamics. There are many potential societal consequences of our work, none which we feel must be specifically highlighted here.

References

- Bai, K., Li, W., Desbrun, M., and Liu, X. Dynamic up-sampling of smoke through dictionary-based learning. *ACM Trans. Graph.*, 40(1), sep 2020. ISSN 0730-0301. doi: 10.1145/3412360. URL <https://doi.org/10.1145/3412360>.
- Bai, K., Wang, C., Desbrun, M., and Liu, X. Predicting high-resolution turbulence details in space and time. *ACM Trans. Graph.*, 40(6), dec 2021. ISSN 0730-0301. doi: 10.1145/3478513.3480492. URL <https://doi.org/10.1145/3478513.3480492>.
- Bertiche, H., Madadi, M., and Escalera, S. Cloth3d: clothed 3d humans. In *European Conference on Computer Vision*, pp. 344–359. Springer, 2020.
- Bogo, F., Romero, J., Pons-Moll, G., and Black, M. J. Dynamic FAUST: Registering human bodies in motion. In *IEEE Conf. on Computer Vision and Pattern Recognition (CVPR)*, July 2017.
- Chu, M., Liu, L., Zheng, Q., Franz, E., Seidel, H.-P., Theobalt, C., and Zayer, R. Physics informed neural fields for smoke reconstruction with sparse data. *ACM Transactions on Graphics*, 41(4):119:1–119:14, aug 2022.
- Eckert, M.-L., Um, K., and Thuerey, N. Scalarflow: A large-scale volumetric data set of real-world scalar transport flows for computer animation and machine learning. *ACM Trans. Graph.*, 38(6), nov 2019. ISSN 0730-0301. doi: 10.1145/3355089.3356545. URL <https://doi.org/10.1145/3355089.3356545>.
- Ferdian, E., Suinesiaputra, A., Dubowitz, D. J., Zhao, D., Wang, A., Cowan, B., and Young, A. A. 4dflownet: Super-resolution 4d flow mri using deep learning and computational fluid dynamics. *Frontiers in Physics*, 8, 2020. ISSN 2296-424X. doi: 10.3389/fphy.2020.00138. URL <https://www.frontiersin.org/articles/10.3389/fphy.2020.00138>.
- Gao, H., Sun, L., and Wang, J.-X. Super-resolution and denoising of fluid flow using physics-informed convolutional neural networks without high-resolution labels. *Physics of Fluids*, 33(7), 2021.
- Graham, J., Kanov, K., Yang, X. I. A., Lee, M., Malaya, N., Lalescu, C. C., Burns, R., Eyink, G., Szalay, A., Moser, R. D., and Meneveau, C. A web services accessible database of turbulent channel flow and its use for testing a new integral wall model for les. *Journal of Turbulence*, 17(2):181–215, 2016. doi: 10.1080/14685248.2015.1088656. URL <https://doi.org/10.1080/14685248.2015.1088656>.
- Guan, S., Deng, H., Wang, Y., and Yang, X. Neurofluid: Fluid dynamics grounding with particle-driven neural radiance fields. In *ICML*, 2022.
- Hoyer, K., Holzner, M., Lüthi, B., Guala, M., Liberzon, A., and Kinzelbach, W. 3d scanning particle tracking velocimetry. *Experiments in Fluids*, 39:923–934, 2005.
- Hu, Y., Fang, Y., Ge, Z., Qu, Z., Zhu, Y., Pradhana, A., and Jiang, C. A moving least squares material point method with displacement discontinuity and two-way rigid body coupling. *ACM Transactions on Graphics*, 37(4):150, 2018.
- Janny, S., Bénéteau, A., Nadri, M., Digne, J., Thome, N., and Wolf, C. EAGLE: Large-scale learning of turbulent fluid dynamics with mesh transformers. In *The Eleventh International Conference on Learning Representations*, 2023. URL <https://openreview.net/forum?id=mfIX4QpsARJ>.
- Keinert, B., Innmann, M., Sängler, M., and Stamminger, M. Spherical fibonacci mapping. *ACM Transactions on Graphics (TOG)*, 34(6):1–7, 2015.
- Kim, B., Azevedo, V. C., Thuerey, N., Kim, T., Gross, M., and Solenthaler, B. Deep fluids: A generative network for parameterized fluid simulations. *Computer Graphics Forum*, 38(2):59–70, 2019. doi: <https://doi.org/10.1111/cgf.13619>. URL <https://onlinelibrary.wiley.com/doi/abs/10.1111/cgf.13619>.
- Lehmann, M. Fluidx3d. URL <https://github.com/ProjectPhysX/FluidX3D>.
- Li, M. and McComb, C. Using physics-informed generative adversarial networks to perform super-resolution for multiphase fluid simulations. *Journal of Computing and Information Science in Engineering*, 22(4):044501, 2022.
- Li, X., Qiao, Y.-L., Chen, P. Y., Jatavallabhula, K. M., Lin, M., Jiang, C., and Gan, C. PAC-neRF: Physics augmented continuum neural radiance fields for geometry-agnostic system identification. In *The Eleventh International Conference on Learning Representations*, 2023. URL <https://openreview.net/forum?id=tVkrbkz42vc>.
- Li, Y., Perlman, E., Wan, M., Yang, Y., Meneveau, C., Burns, R., Chen, S., Szalay, A., and Eyink, G. A public turbulence database cluster and applications to study lagrangian evolution of velocity increments in turbulence. *Journal of Turbulence*, 9(31), 2008.

- Li, Y., Takehara, H., Taketomi, T., Zheng, B., and Nießner, M. 4dcomplete: Non-rigid motion estimation beyond the observable surface. *IEEE International Conference on Computer Vision (ICCV)*, 2021.
- Li, Z. and Farimani, A. B. Graph neural network-accelerated lagrangian fluid simulation. *Computers & Graphics*, 103: 201–211, 2022.
- Lino, M., Fotiadis, S., Bharath, A. A., and Cantwell, C. D. Current and emerging deep-learning methods for the simulation of fluid dynamics. *Proceedings of the Royal Society A*, 479(2275):20230058, 2023.
- Loper, M., Mahmood, N., Romero, J., Pons-Moll, G., and Black, M. J. SMPL: A skinned multi-person linear model. *ACM Trans. Graphics (Proc. SIGGRAPH Asia)*, 34(6): 248:1–248:16, October 2015.
- Mildenhall, B., Srinivasan, P. P., Tancik, M., Barron, J. T., Ramamoorthi, R., and Ng, R. Nerf: Representing scenes as neural radiance fields for view synthesis. In *ECCV*, 2020.
- Patel, C., Liao, Z., and Pons-Moll, G. Tailornet: Predicting clothing in 3d as a function of human pose, shape and garment style. In *IEEE Conference on Computer Vision and Pattern Recognition (CVPR)*. IEEE, jun 2020.
- Perlman, E., Burns, R., Li, Y., and Meneveau, C. Data exploration of turbulence simulations using a database cluster. In *SC '07: Proceedings of the 2007 ACM/IEEE Conference on Supercomputing*. Association for Computing Machinery, 2007.
- Pfaff, T., Fortunato, M., Sanchez-Gonzalez, A., and Battaglia, P. Learning mesh-based simulation with graph networks. In *International Conference on Learning Representations*, 2021. URL https://openreview.net/forum?id=roNqYL0_XP.
- Prantl, L., Ummenhofer, B., Koltun, V., and Thuerey, N. Guaranteed conservation of momentum for learning particle-based fluid dynamics. In *Conference on Neural Information Processing Systems*, 2022.
- Scarselli, F., Gori, M., Tsoi, A. C., Hagenbuchner, M., and Monfardini, G. The graph neural network model. *IEEE transactions on neural networks*, 20(1):61–80, 2008.
- Stachenfeld, K., Fielding, D. B., Kochkov, D., Cranmer, M., Pfaff, T., Godwin, J., Cui, C., Ho, S., Battaglia, P., and Sanchez-Gonzalez, A. Learned simulators for turbulence. In *International Conference on Learning Representations*, 2022. URL <https://openreview.net/forum?id=msRBojTz-Nh>.
- Toshev, A. P. and Adams, N. A. Lagrangebench datasets, October 2023. URL <https://zenodo.org/doi/10.5281/zenodo.10021925>.
- Toshev, A. P., Galletti, G., Fritz, F., Adami, S., and Adams, N. A. Lagrangebench: A lagrangian fluid mechanics benchmarking suite. In *37th Conference on Neural Information Processing Systems (NeurIPS 2023) Track on Datasets and Benchmarks*, 2023. URL <https://arxiv.org/abs/2309.16342>.
- Ummenhofer, B., Prantl, L., Thuerey, N., and Koltun, V. Lagrangian fluid simulation with continuous convolutions. In *International Conference on Learning Representations*, 2020.
- Vinuesa, R. and Brunton, S. L. Enhancing computational fluid dynamics with machine learning. *Nature Computational Science*, 2(6):358–366, 2022.
- Wang, Z., Yang, W., Cao, J., Xu, L., ming Yu, J., and Yu, J. Neref: Neural refractive field for fluid surface reconstruction and implicit representation. *ArXiv*, abs/2203.04130, 2022. URL <https://api.semanticscholar.org/CorpusID:247315295>.
- Werhahn, M., Xie, Y., Chu, M., and Thuerey, N. A multi-pass gan for fluid flow super-resolution. *Proc. ACM Comput. Graph. Interact. Tech.*, 2(2), jul 2019. doi: 10.1145/3340251. URL <https://doi.org/10.1145/3340251>.
- Wiewel, S., Becher, M., and Thuerey, N. Latent space physics: Towards learning the temporal evolution of fluid flow. In *Computer graphics forum*, volume 38, pp. 71–82. Wiley Online Library, 2019.
- Wiewel, S., Kim, B., Azevedo, V., Solenthaler, B., and Thuerey, N. Latent space subdivision: Stable and controllable time predictions for fluid flow (2020). *arXiv preprint arXiv:2003.08723*, 2020.
- Xie, Y., Franz, E., Chu, M., and Thuerey, N. tempogan: A temporally coherent, volumetric gan for super-resolution fluid flow. *ACM Transactions on Graphics (TOG)*, 37(4): 95, 2018.